

# Experimental Study of Laser-Initiated Radiofrequency-Sustained High-Pressure Plasmas

Siqi Luo, *Member, IEEE*, John E. Scharer, *Senior Member, IEEE*,  
Magesh Thiagarajan, *Student Member, IEEE*, and C. Mark Denning, *Member, IEEE*

**Abstract**—Experiments are performed using 193-nm ultraviolet laser preionization of a seed gas in atmospheric pressure range argon and nitrogen to initiate a discharge that is sustained by 13.56-MHz radiofrequency (RF) power using efficient inductive wave coupling. High-density ( $4.5 \times 10^{12}/\text{cm}^3$  line average density) large-volume ( $\sim 500 \text{ cm}^3$ ) 760-torr argon plasma is initiated and maintained for more than 400 ms with 2.2 kW of net RF power coupled to the plasma. Using the same technique, a 50-torr nitrogen plasma with line average electron density of  $3.5 \times 10^{11}/\text{cm}^3$  is obtained. The nitrogen plasma volume of  $1500 \text{ cm}^3$  is initiated by the laser and maintained by a net RF power of 3.5 kW for 350 ms. Measurements of the time-varying plasma impedance and optimization of the RF matching for the transition from laser-initiated to RF-sustained plasma are carried out. Both laser-initiated plasmas provide much larger plasma volumes at lower RF power densities than can be obtained by RF alone. Millimeter wave interferometry is used to determine the electron density and the total electron–neutral collision frequency. A new diagnostic technique based on interferometry is developed to evaluate the electron temperature in high-pressure plasmas with inclusion of the neutral heating. Broadband plasma emission spectroscopy is used to illustrate the changes in the ionized species character immediately after the laser pulse and later during the RF pulse.

**Index Terms**—Excimer laser, high pressure, interferometry, plasma, radiofrequency (RF).

## I. INTRODUCTION

HIGH-PRESSURE inductively coupled plasmas (ICPs) have been used for a variety of scientific and industrial applications over a large gas pressure range from tens of torr up to and beyond atmospheric pressures. For this plasma source, a helical antenna coil is used to couple radiofrequency (RF) power to the plasma using a capacitive impedance matching network. The applications of these plasmas require high-density ( $\sim 10^{11-13} \text{ cm}^{-3}$ ), uniform plasmas over large volumes ( $\sim 1000 - 5000 \text{ cm}^3$ ) with a reduced RF power budget. Atmospheric pressure plasmas can be used in open space for a

variety of applications including materials processing [1], biological decontamination [2], microwave reflector and absorber [3], [4], reduction of supersonic drag, and modification of the radar cross section and signature of an aircraft [5]. An up-to-date summary of atmospheric plasmas is available in a recent book entitled *Non-Equilibrium Air Plasmas at Atmospheric Pressure* [6].

One of the major challenges associated with such high-pressure plasma sources is the high-RF-power budget required to initiate large volumes of these discharges at high density. The minimum theoretical power density per unit volume required to initiate an air plasma density of  $10^{13} \text{ cm}^{-3}$  at sea level (760 torr) has been calculated to be  $9 \text{ kW}/\text{cm}^3$  [7]. The primary reason for the increased power budget is that under high pressure and high neutral concentrations, the frequency of inelastic processes (especially the recombination process) between electrons and neutrals is much higher than for lower pressure plasma cases, greatly reducing the lifetime of energetic free electrons. As a result, it becomes very difficult to use RF electric fields to accelerate electrons to sufficiently high kinetic energies to ionize neutrals and initiate a large volume plasma discharge unless a high field intensity is created.

The collisional ( $\nu \gg \omega_{\text{RF}}$ ) skin depth for RF penetration in an unmagnetized plasma is given by  $\delta = \sqrt{2}(c/\omega_{\text{p}})(\nu/\omega_{\text{RF}})^{1/2}$  m where  $\nu$  is the total electron–neutral collision frequency,  $c$  is the speed of light in vacuum,  $\omega_{\text{RF}}$  is the RF frequency (13.56 MHz for our case), and  $\omega_{\text{p}}$  is the electron plasma frequency. The skin depth is larger for higher total collision frequencies, lower densities, and lower RF frequencies. The RF penetration depth, field strength, and ionization at a given plasma density and total collision frequency will be larger for lower RF frequencies than for microwaves [8]–[10].

In a classic experiment, Eckert and Kelly [11] created an atmospheric pressure plasma by initiating the RF-only discharge at a low pressure (1 torr) in both argon and air and slowly raising the pressure over time. They studied the emission spectrum produced by the high-pressure plasma and determined the plasma density and temperature. Following the work of Babat [12], they created a plasma using an inductive coil at a lower pressure and slowly increased the neutral pressure and RF power until they could open the plasma chamber to the atmosphere. To protect the quartz chamber from heat damage and to help stabilize the discharge, the gas was injected in a vortex, essentially forming a thermal gas barrier between the hot plasma

Manuscript received December 8, 2005; revised July 7, 2006. This work was supported by the Air Force Office of Scientific Research (AFOSR) under Grant F49620-03-1-0252.

The authors are with the Department of Electrical and Computer Engineering, University of Wisconsin-Madison, WI 53706 USA (e-mail: siqiluo@wisc.edu; scharer@engr.wisc.edu).

Color versions of Figs. 6, 7, and 14 are available at <http://ieeexplore.ieee.org>. Digital Object Identifier 10.1109/TPS.2006.885096

and the chamber wall. The coupled power required to maintain the discharge was 18–50 kW at 4 MHz, sufficient to create the plasma at lower pressure and sustain it up to atmospheric pressure with a large volume. The time scale for creating the high-pressure plasma from the initial low-pressure discharge was several minutes. They used the spectroscopic diagnostic of the  $N_2$  second positive ( $N_2(2+)$ ) line ratio to obtain an electron temperature of  $T_e = 0.62$  eV and  $T_n = 6300$  K for 760-torr air. By observing Stark broadening of the  $H_\beta$  line in the air plasma, they found the electron density to be  $5 \times 10^{14} \text{ cm}^{-3}$  in the air plasma created. More recently, experimental and computational modeling work has been done on a high power density and plasma density RF inductively coupled air and argon/nitrogen plasma torch by Laux [6, pp. 395–407], [13], [14]. They utilize a wide spectrum of techniques including spectroscopy (OH and  $N_2^+$  emissions, especially) and chemical kinetic models to study the RF plasmas generated in fast-injected (100 standard liters per minute (SLM) through the torch) air and nitrogen. In Laux's work, plasmas with higher electron densities ( $n_e$  on the order of  $10^{14}/\text{cm}^3$ ) and smaller volumes are created and sustained with higher RF power density ( $105 \text{ W}/\text{cm}^3$ ). Gas temperatures of several thousand  $K$  are observed among other results.

Currently, there is substantial interest in a rapid, almost instantaneous initiation of large-volume ( $\sim 1000 \text{ cm}^3$ ) high-density ( $10^{11} - 10^{13} \text{ cm}^{-3}$ ) discharges at atmospheric pressures (50–760 torr, corresponding to altitudes of 60 000 ft down to sea level) with a minimal steady-state RF power budget. The power required in an experiment to ionize and initiate an inductively coupled RF plasma in atmospheric pressure air at a density of  $10^{13} \text{ cm}^{-3}$  will be much higher than the theoretical minimum power level ( $\sim 9 \text{ kW}/\text{cm}^3$ ). For an atmospheric pressure plasma arc torch, a 300-kV potential was required to initiate a discharge, whereas only 100 V is needed to maintain the discharge with operating currents of 200–600 A [15], [16]. Therefore, there is a need for an alternative scheme to reduce the power budget required to sustain the pulsed plasma at high gas pressures. We envisioned that if we could ionize a seed gas with a low ionization energy such as tetrakis (dimethylamino) ethylene (TMAE) (ionization energy 6.1 eV) by ultraviolet (UV) laser or flashtube photon absorption [17]–[19], then we could efficiently couple electrodeless RF power to the plasma at high gas pressures and sustain the plasma at greatly reduced RF power levels [20].

We have thus focused on developing an electrodeless method for creating a large-volume (greater than  $500 \text{ cm}^3$ ) seed plasma using UV photoionization to provide a good load for efficient RF coupling at low RF power levels via pulsed inductively coupled sources. Previous experiments [17]–[19] have shown that a high initial density TMAE plasma ( $10^{12-13} \text{ cm}^{-3}$ ) of long axial extent ( $\sim 100 \text{ cm}$ ) can be created by a 193-nm laser in 760 torr of nitrogen, air, oxygen, or argon background gas. We have been able to create a quasi-steady-state high-pressure plasma that projects well away from the antenna by this means that could not be obtained by RF alone. The technique of initiating a discharge by 193-nm-laser photoionization of TMAE seeded in high-pressure background argon gas that is sustained by inductive coupling of reduced RF power at

moderate pressures ( $< 120$  torr) has been demonstrated by Kelly *et al.* [18], [20]. While we have utilized a laser to perform the preionization, a more compact and lower power UV flash tube scheme could also be used to initiate the seeded plasma.

The objective of this paper is to utilize the UV-laser-initiated axially extended high-density seed plasma to help overcome the initial high-RF-power requirement to breakdown high-pressure gas and create an RF-sustained high-pressure argon or nitrogen plasma through improved inductive RF power coupling and increased RF wave penetration. Another characteristic of the plasma created with the help of laser initiation is its possible deviation from thermal equilibrium. We anticipated that the laser formed seed plasma could allow for further RF penetration, higher plasma density and larger plasma volumes compared with RF-only initiated plasmas.

A 105-GHz millimeter wave interferometer is employed to determine the line-average plasma density, total electron–neutral collision frequency, and electron temperature using a new analysis method. Optical emission spectroscopy is used to characterize the temporal evolution of the plasma. A technique to measure the time-dependent, plasma-loaded antenna impedance  $Z_p(t)$ , during an RF plasma pulse using a dual RF directional coupler, which can be used for precise capacitive matching to the plasma load, is also presented.

This paper is organized as follows: a brief theoretical analysis of the laser-initiated RF-sustained plasma is presented in Section II, followed by a description of the experimental configuration and theory for the plasma diagnostics in Section III; the experimental results are discussed in Section IV, and Section V provides a summary with discussions.

## II. THEORETICAL ANALYSIS OF THE UNMAGNETIZED PLASMA

### A. Electron and Neutral Thermal Energy

In this section, we present a theoretical analysis of the laser-initiated and RF-sustained plasma based on an energy conservation principle. By creating an excimer laser preionized seed plasma, a quasi-steady-state RF plasma is created and sustained. Due to the RF plasma impedance mismatch, a fraction of the incident RF power ( $P_{\text{inc}}$ ) is delivered to the helical antenna as  $P_{\text{net}}$  while the rest is reflected back to the RF generator ( $P_{\text{ref}}$ ). Only part of the power coupled to the antenna,  $P_e = e_r P_{\text{net}}$  is coupled to the plasma electrons through azimuthal field coupling

$$P_e = \iiint_V \frac{1}{2} j_\theta E_\theta dV = e_r P_{\text{net}} \quad (1)$$

where the  $1/2 j_\theta E_\theta$  term is the RF power density coupled to the plasma from the inductive coil, with  $j_\theta$  being the azimuthal plasma current and  $E_\theta$  the azimuthal electric field.  $V$  is the volume of plasma, and  $e_r$  is the antenna radiation efficiency. Not all the RF power delivered to the helical antenna is coupled into plasma, as some is dissipated by contact resistance in the matching system and antenna, the Ohmic heating of the antenna

(skin effect) (denoted by  $e_{\text{Ohm}}$ ), and radiation loss into the outside RF field (denoted by  $e_{\text{Rad}}$ ) [21]

$$e_r = \frac{P_e}{P_{\text{net}}} = e_{\text{Ohm}} e_{\text{Rad}}. \quad (2)$$

We use a circuit measurement and analysis technique to calculate  $e_{\text{Ohm}}$  and  $e_{\text{Rad}}$ . We first measure the matchbox series resistance and vacuum antenna resistance using an HP E5061A ENA-L RF network analyzer, and then measure the plasma impedance of argon and nitrogen plasma using the dual RF directional coupler.  $e_{\text{Ohm}}$  and  $e_{\text{Rad}}$  are then calculated using Kirchoff's law. This method is used in Part IV for coupled RF power and electron temperature analysis.

The RF power coupled to the plasma is coupled to numerous power consumption and loss mechanisms that are represented by different terms in (3), the complete differential form of the energy conservation equation for electrons [8], [22]–[24]

$$\begin{aligned} & \frac{\partial}{\partial t} \left( \frac{3}{2} n_e T_e \right) + \nabla \cdot \frac{3}{2} n_e T_e \mathbf{u}_e \\ &= -\nabla \cdot (K_e \nabla T_e + h_e \mathbf{J}_e) - p_e \nabla \cdot \mathbf{u}_e + \frac{\mathbf{J}_e}{n_e} \cdot \nabla p_e \\ & - \dot{Q}_{\text{elastic,e-n}} + \sum_r R_{er} \Delta H_r^o + \frac{1}{2} j_\theta E_\theta \end{aligned} \quad (3)$$

where  $n_e$  is the electron density,  $T_e$  is electron temperature,  $\mathbf{u}_e$  is the convection velocity,  $K_e$  is the thermal conductivity of electrons,  $h_e$  is the specific enthalpy of electrons,  $\mathbf{J}_e$  is the diffusion flux of electrons, and  $p_e$  is the electron pressure. Equation (3) illustrates the radiation, heat conduction and convection, dissociation, and ionization processes that compete with neutral heating via electron–neutral collisions. The first term on the left-hand side is the temporal variation of electron thermal energy, which can be neglected in our quasi-steady-state plasma; the second term is the convective energy transport term. The first term on the right-hand side is the sum of thermal conduction and diffusion, the two terms that follow are volume work, and the  $\dot{Q}_{\text{elastic,e-n}}$  term represents the energy transfer rate between electrons and neutrals. Based on an elastic collision model for energy transfer from electrons to neutrals [8, p. 55], [23, p. 145], [25],  $\dot{Q}_{\text{elastic,e-n}}$  can be approximated as  $\dot{Q}_{\text{elastic,e-n}} = E_{\text{eav}} \nu_e \cdot 2(m_e/M_n) n_e = T_e \nu_e \cdot 3(m_e/M_n) n_e$  in which  $E_{\text{eav}}$  is the average electron energy ( $E_{\text{eav}} = 3/2 k_B T_e$  for electrons in a three-dimensional (3-D) Maxwellian distribution),  $m_e$  is the electron mass,  $M_n$  is the neutral mass, and  $\nu_e$  is the frequency of elastic electron–neutral collisions.  $T_e$  is the line average electron temperature and  $2(m_e/M_n)$  is the fraction of electron kinetic energy transferred to neutrals during each elastic collision. The  $\sum_r R_{er} \Delta H_r^o$  term stands for the sum of reactive energy released or absorbed by various reactions. Some of the energy loss via reactions can leave the plasma system as radiation via photon emission. The  $1/2 j_\theta E_\theta$  term is the energy source term from incoming RF power. The gas flow through the chamber also removes RF power and cools the neutrals, which we neglect because the gas flow rate is small compared with the electron heating rate and total gas volume in the chamber. We can simplify the energy

relation for electrons by introducing an efficiency coefficient  $\eta_e$  defined as the fraction of RF power that is consumed by elastic collisions with the neutrals:

$$\dot{Q}_{\text{elastic,e-n}} = \eta_e \cdot \frac{1}{2} j_\theta E_\theta \quad (4)$$

and  $(1 - \eta_e)$  of the RF power coupled to the electrons is consumed by the other competing power consumption mechanisms listed above. We designate  $\eta_e$  as the elastic collision factor.

As electrons gain their thermal energy through the interaction with the RF electric field and transfer a fraction of their energy to neutrals through elastic collisions, the neutral gas will gain some of the thermal energy through the elastic collision process. Hence, the  $\dot{Q}_{\text{elastic,e-n}}$  term is the energy source for the thermal energy gain of the neutrals. The differential form of the energy equation for neutrals is [22], [24]

$$\begin{aligned} & \frac{\partial}{\partial t} \left( \frac{3}{2} n_n T_n \right) + \nabla \cdot \frac{3}{2} n_n T_n \mathbf{u}_n \\ &= -\nabla \cdot (K_n \nabla T_n + h_n \mathbf{J}_n) - p_n \nabla \cdot \mathbf{u}_n \\ & + \frac{\mathbf{J}_n}{n_n} \cdot \nabla p_n + \dot{Q}_{\text{elastic,e-n}} + \sum_r R_{nr} \Delta H_r^o. \end{aligned} \quad (5)$$

All the terms are similar to those in the electron energy (1), with two exceptions: 1) the sign of the  $\dot{Q}_{\text{elastic,e-n}}$  term is positive because neutrals gain thermal energy from the electrons via elastic collisions and 2) the absence of  $1/2 j_\theta E_\theta$  term. Not all of the thermal energy available from electrons is transferred to heating neutrals through collisions ( $\dot{Q}_{\text{elastic,e-n}}$ ); part of it is consumed by radiation, diffusion, convection, conduction, cooler gas flow in and warm neutral pumping out of the system, and neutral emission energy losses. We further simplify (5) by introducing another efficiency factor: The neutral heating factor  $\eta_n$  which stands for the ratio of elastically transferred energy that does contribute to heating of neutrals [22], [24]

$$\frac{\partial}{\partial t} \left( \frac{3}{2} n_n T_n \right) + p_n \nabla \cdot \mathbf{u}_n - \frac{\mathbf{J}_n}{n_n} \cdot \nabla p_n = \eta_n \dot{Q}_{\text{elastic,e-n}}. \quad (6)$$

If we use the constant-pressure specific heat  $C_p$  to incorporate volume work by neutrals, (6) can be rewritten in this form

$$C_p n_n \frac{\partial T_n}{\partial t} = e_r \eta \frac{1}{2} j_\theta E_\theta. \quad (7)$$

The total neutral heating efficiency factor  $\eta = \eta_n \eta_e$  is defined as the ratio of RF power density that ultimately contributes to thermal temperature rise of neutrals. In effect, the electrons in high-pressure plasmas act as intermediaries that transfer some of the RF power to the neutrals and heat them to elevated temperatures [11]. We note that the process of gas heating arising from the electrons in the experiment competes with many other power loss processes including plasma ionization, dissociation, excitation, recombination, radiation, cooler gas flow in and pumping out of the system, and heat transfer to the Pyrex walls and regions of gas surrounding the plasma by means of convection, conduction, diffusion, and radiation. The reaction mechanisms are given in [25] and [26] for argon

and nitrogen plasmas. As a result that follows other referenced computational modeling neutral heating papers [22], [24], [25], we define the total neutral heating efficiency factor  $\eta$  as the ratio of RF power density that contributes to the temperature rise of neutrals. The choice of the  $\eta$  factor is of special importance:  $\eta$  is dependent on the gas and the reaction mechanisms involved. Experimental and detailed computational modeling research work has been done on neutral heating effect in ICP sources in [22], [24], and [25] at pressures up to 0.5 torr. For different gas species, pressure levels, electron energy levels and RF power density levels involved, different  $\eta$  factors for different gases ranging from 5% to 30% have been employed as referenced by Hash *et al.* [22] and result in electron temperatures well above the gas temperature. Because our experiments are conducted in the 50–760-torr pressure range with laser-initiation and RF-sustainment technique, no  $\eta$  factor has been evaluated for this pressure and plasma density range. In the absence of a complex, detailed computational model that includes the reactions listed in [25] and [26], and all the thermal dynamics processes that competes with neutral heating, or a spectroscopic study of this neutral temperature change for our special case of a laser-initiated RF-sustained lower power and electron density plasma, we take  $\eta = 40\%$  for the 760-torr argon plasma, and  $\eta = 20\%$  for the nitrogen plasma.  $\eta$  is assumed to be higher (40%) for 760-torr argon plasma because at this pressure, the electron–neutral collision process provides a higher neutral heating efficiency, and being a noble gas, argon has less additional power-consuming reactions compared to the nitrogen gas species.  $\eta$  is chosen at a level of 20% for the nitrogen plasma due to the lower pressure of operation (50 torr), lower plasma density and additional competing power balance reactions involved in producing the plasma [26].

The ideal gas law is also valid for the neutrals

$$p_n = n_n k_B T_n \quad (8)$$

where  $p_n$  is the neutral pressure measurable using our piezo-electric pressure gauge,  $k_B$  is Boltzmann's constant, and  $n_n$  is the neutral density. Equations (7) and (8) can be used to evaluate the neutral temperature and density changes as a result of neutral heating. With these conditions and assumptions, we then evaluate the neutral heating that can occur and include it in the evaluation of the line-average electron temperatures. The results are presented in Section IV.

### B. Electron–Neutral Collisions

The total electron–neutral collision frequency is given by [8, p. 47], [27, p. 157]:

$$\nu = \sigma n_n \bar{v} \quad (9)$$

in which  $\sigma$  is the total electron collision cross section between electrons and neutrals and  $\bar{v}$  is the average velocity of the electrons. Note that the total cross section  $\sigma$  is a function of the average electron energy (again,  $E_{\text{eav}} = 3/2 k_B T_e$  for electrons in a 3-D Maxwellian distribution): the curves illustrating this dependence for various gases are summarized by Shkarofsky in [28] and more recently by Zecca in [29].  $\bar{v}$  is related to electron

temperature  $T_e$  by (10) if we assume a 3-D near-Maxwellian velocity distribution for the electrons [8, p. 39], [27, p. 228]:

$$\bar{v} = \left( \frac{8k_B T_e}{\pi m_e} \right)^{1/2} \quad (10)$$

Eliminating  $\bar{v}$ , we can combine (9) and (10) to write

$$k_B T_e = \frac{\pi m_e}{8} \left( \frac{\nu}{\sigma n_n} \right)^2. \quad (11)$$

This equation can be used to evaluate the line average  $T_e$  with  $n_n$  obtained using (7) and (8), and  $\nu$  obtained using our interferometer diagnostic.

## III. EXPERIMENT

### A. Overview of Excimer Laser, Plasma Chamber, and RF Power Coupling

The experimental set up is shown schematically in Fig. 1. The plasma chamber is a 5-cm-inner-diameter Pyrex tube of length 140 cm. Mass flow controllers along with a gas injection system are located at the laser window end as shown in Fig. 1. The chamber is evacuated to a base pressure of 50 mtorr prior to each experiment. After evacuation, a stable chamber pressure is achieved by fine tuning and balancing the gas input valve and throttle valve of the mechanical pump to control gas input rate and pumping rate. A thermal gas flow meter (McMillan Model 50S) located at the gas injection pipeline is used to measure the incoming gas flow rate. A piezomicroelectromechanical-systems-based pressure gauge (MKS HPS Series 902 Absolute Piezo Transducer) is used to monitor the chamber pressure accurately from 100 mtorr to 1000 torr. Typical gas flow rates range from 0.5 to 5.0 SLM. After a steady chamber pressure and flow rate is established, TMAE is injected into the chamber. Prior to injection, the TMAE cylinder is pressurized with the background gas at 5 torr above the gas pressure in the main chamber. For fast injection of TMAE, an electromechanical valve is opened for 1 s, so that an optimum TMAE gas partial pressure of 15 mtorr [17] is achieved in the chamber and the laser-RF sequence is initiated several seconds later.

A 25-kW 13.56-MHz radio-frequency generator (CXH25K, Comdel, Inc.) is used to deliver power to the antenna using an efficient capacitive impedance matching network. This generator is a tube-powered unit capable of putting out 5-kW incident RF power even with the output end shorted. The short (20 ns) laser pulse is triggered late during the initial rise of the RF when the forward RF power is 90% of the maximum power, in order to provide the seed plasma for efficient RF coupling and sustainment at low RF power levels. A dual directional coupler (Connecticut Microwave) with 50-dB incident and 40-dB reflected coupling is used to measure the incident and reflected voltage ( $V_{\text{inc}}$  and  $V_{\text{ref}}$ ) to determine the plasma load impedance  $Z_p(t)$  defined at the feed points to the six-turn helical antenna. The RF power is coupled through a helical antenna that excites RF fields in the laser-formed plasma. The water-cooled helical antenna is made of six turns of quarter-inch copper tube of axial coil length 10 cm and internal diameter 6 cm, wound

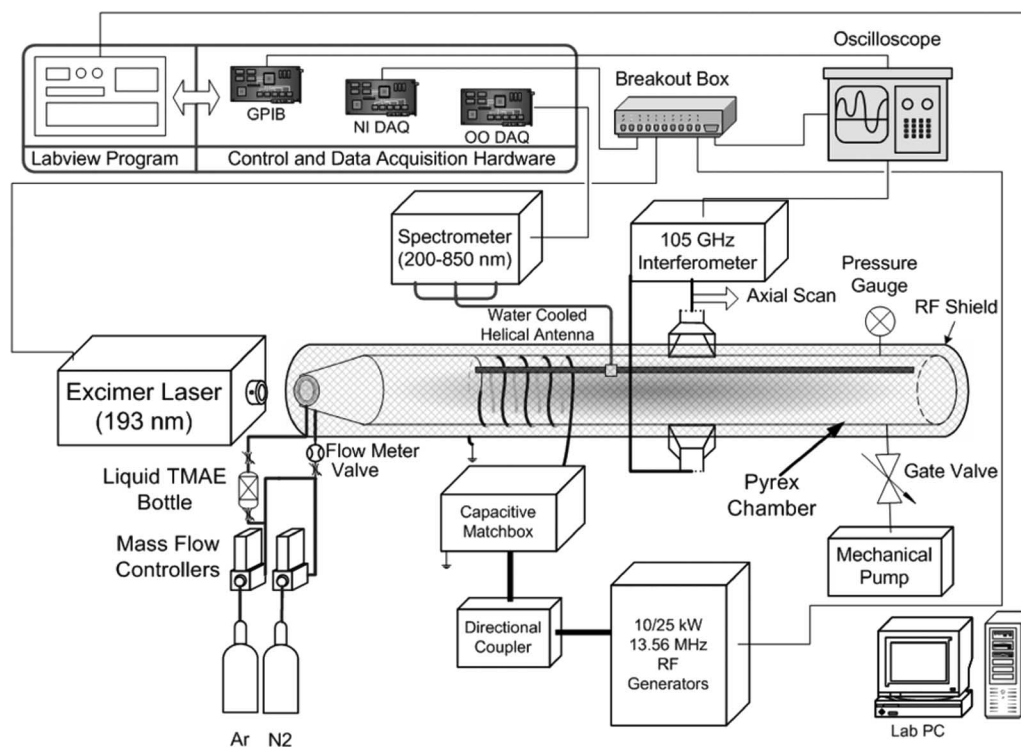


Fig. 1. Experimental configuration of the laser and RF plasma source.

tightly over the 5-cm-inner-diameter chamber. The end of the helical antenna closest to the laser window is grounded to the capacitive match box. The high-voltage lead of the helix is toward the pump side of the chamber. Radio frequency power is coupled to the capacitive impedance matching network using a 1-5/8", 50- $\Omega$  semirigid coaxial transmission line (Myat, Inc.).

The capacitive matching network consists of two high-working-voltage vacuum variable capacitors (Jennings GCS 100-7.5S, 5-100 pF, 7.5 kV, and Jennings CVFP-1000-40S, 35-1000 pF, 40 kV). The capacitances and series and contact resistances of the two variable capacitors are determined by network analyzer. A lookup table with these values can be used to either determine the capacitance or tune to a desired capacitance based on the number of turns. The two-capacitor matching circuit and wide (4 in) interconnect copper strips which are chosen to reduce inductance and skin effect losses are enclosed in an aluminum box to provide RF shielding. The range of plasma radiation resistance at the antenna terminals (0.5-5  $\Omega$ , confirmed by measurement of the plasma radiation impedance in our experiment) mandates special care to reduce ohmic losses in the impedance matching network and connections. To reduce RF losses arising from connection points and solder joints, the six-turn helical antenna has been made out of a continuous length of copper tube with a measured equivalent vacuum series resistance of 0.5  $\Omega$  due to skin effect, contact resistance and radiation resistance into vacuum.

A uniform intensity UV beam of 193-nm wavelength is produced using an excimer laser (Lumonics Pulsemaster PM-842) that runs in the ArF (6.4 eV per photon) mode. The half-width of the laser pulse is  $20 \pm 2$  ns, with a 2 ns rise/fall time, a maximum available laser output energy of 300 mJ, and a typical working output of 100 mJ. The uniform laser flux output

cross section is  $2.8 \times 1.2$  cm. The laser beam enters the plasma chamber through a 2.8-cm diameter Suprasil quartz window (98% transparency at 193-nm wavelength) at the upstream end. Laser energy passing through the UV window is measured using an energy meter (Scientech AC 50 UV Calorimeter and Astral AD30 Laser Energy Meter). In order to account for the laser attenuation by the UV window, the window is placed in front of the energy meter for this measurement.

A very accurate computer-controlled timing circuit sequences RF turn-ON and turn-OFF, laser firing, and data acquisition. This exact timing sequence is very critical since the RF pulse must be enabled during the laser-formed TMAE plasma lifetime ( $\tau \sim 3 \mu\text{s}$ ) where the seed plasma density is sufficiently large ( $n_e > 10^{12}/\text{cm}^3$ ) [17] to provide a sufficient plasma radiation resistance load ( $R_p > 1 \Omega$ ) for efficient RF coupling through the helical antenna. Due to the long rise time of the tube powered RF generator, we trigger the laser pulse when the RF power is ramped to approximately 90% of full power, so that the laser-initiated plasma can be sustained by high RF power.

### B. Millimeter Wave Interferometry at High Gas Pressures

A 105-GHz quadrature millimeter wave interferometer is used to measure the electron plasma frequency ( $\omega_p$ ), plasma density ( $n_e$ ), total electron-neutral collision frequency ( $\nu$ ), and electron temperature ( $T_e$ ) at high neutral gas pressures. The interferometer works in the Mach-Zehnder configuration, in which the plasma is in one arm of the two-beam interferometer. The interferometer works by using an I-Q (In-phase and Quadrature-phase) mixer to determine the phase and amplitude change of the 105-GHz wave signal going through the plasma

with reference to the wave that does not go through the plasma ([17], [18], and [30]). An oscilloscope is used to acquire the signals from the interferometer, which are then transferred to a computer for analysis. As much of the interferometer assembly as possible is enclosed in a conducting shielding box, only the waveguide horns and phase shifter are exposed. In addition, cables with very high shielding (90 dB, Times Microwave Systems) have been used to reduce the noise level from the laser and RF sources in the interferometer signal. An axial density scan is obtained by varying the position of the interferometer along the  $z$ -axis.

The objective of the plasma interferometry experiment is to accurately diagnose the high-pressure plasma over the entire pulse. A new approach has been developed and employed to evaluate the plasma characteristics  $\nu$ ,  $\omega_p$ ,  $n_e$ , and  $T_e$ , based on the millimeter wave interferometry. Given a plasma with a total electron-neutral collision frequency ( $\nu$ ) and plasma frequency ( $\omega_p$ ), if we launch a plane wave through the plasma, which is assumed to be infinite in dimensions transverse to the direction of microwave propagation and has thickness  $d$  along the direction of propagation, the phase constant  $\beta_p$  and attenuation constant  $\alpha_p$  of the wave are [30]

$$\beta_p = \frac{\omega}{c} \left\{ \frac{1}{2} \left( 1 - \frac{\omega_p^2}{\omega^2 + \nu^2} \right) + \frac{1}{2} \left[ \left( 1 - \frac{\omega_p^2}{\omega^2 + \nu^2} \right)^2 + \left( \frac{\omega_p^2 \nu}{\omega^2 + \nu^2 \omega} \right)^2 \right]^{1/2} \right\}^{1/2} \quad (12)$$

$$\alpha_p = \frac{\omega}{c} \left\{ -\frac{1}{2} \left( 1 - \frac{\omega_p^2}{\omega^2 + \nu^2} \right) + \frac{1}{2} \left[ \left( 1 - \frac{\omega_p^2}{\omega^2 + \nu^2} \right)^2 + \left( \frac{\omega_p^2 \nu}{\omega^2 + \nu^2 \omega} \right)^2 \right]^{1/2} \right\}^{1/2} \quad (13)$$

in which  $\omega$  is the frequency of the millimeter wave interferometer signal. Both  $\nu$  and  $\omega_p$  are plasma characteristics which are functions of spatial location within the plasma at any given time. They can therefore be written as  $\nu(z, r, \theta, t)$  and  $\omega_p(z, r, \theta, t)$ , where we use cylindrical coordinates due to chamber geometry. Both  $\nu$  and  $\omega_p$  are local characteristics of the plasma. There exist radial as well as axial profiles for plasma density and total electron-neutral collision frequency. Note that since  $\beta_p$  and  $\alpha_p$  are determined by  $\nu$  and  $\omega_p$ , they are local values and therefore also have a spatial variation. However, the interferometry method measures the phase shift and attenuation as integration over the entire wave path

$$\Delta\varphi = \int_0^d (\beta_0 - \beta_p) dx \quad (14)$$

$$A = A_0 e^{\int_0^d (\alpha_0 - \alpha_p) dx} \quad (15)$$

because the 105-GHz microwave beam penetrates through the entire plasma column and experiences a total phase shift and attenuation. Here,  $\alpha_0$  is the attenuation constant of air ( $\alpha_0 \approx 0$ ),  $\beta_0$  is the phase constant of free space,  $d$  is the diameter of plasma chamber, and  $x$  is the integration variable.  $\Delta\varphi$  is the phase shift,  $A_0$  is the initial amplitude, and  $A$  is the amplitude of the microwave after the attenuation effect by the plasma.

Since it is impractical to measure the radial profile of  $\nu$  and  $n_e$  in an atmospheric-pressure plasma, we assume a one-dimensional (1-D) plasma slab model with a radial profile assumed uniform due to the high recombination rates. As a result, the integrations in (16) and (17) can be simplified into multiplication

$$\Delta\varphi = (\beta_0 - \beta_p)d \quad (16)$$

$$A = A_0 e^{-\alpha_p d}. \quad (17)$$

This 1-D uniform plasma slab model is conservative in predicting the peak density and collision rate because it ignores the effect that the chamber wall will have on the plasma and assumes a uniform radial profile of  $\nu$  and  $\omega_p$  within the plasma.

Notice that (14) and (15) are explicit expressions of  $\beta_p$  and  $\alpha_p$  in terms of  $\nu$  and  $\omega_p$ . In order to make use of the experimentally measured values for  $\alpha_p$  and  $\beta_p$ , it is necessary to invert these equations to produce explicit expressions for  $\nu$  and  $\omega_p$ . First, let us define two intermediate variables  $X$  and  $Y$  given by

$$X = \frac{1}{2} \left( 1 - \frac{\omega_p^2}{\omega^2 + \nu^2} \right) \quad (18)$$

$$Y = \frac{1}{2} \left[ \left( 1 - \frac{\omega_p^2}{\omega^2 + \nu^2} \right)^2 + \left( \frac{\omega_p^2 \nu}{\omega^2 + \nu^2 \omega} \right)^2 \right]^{1/2} \\ = \frac{1}{2} \left[ (2X)^2 + \left( \frac{\omega_p^2 \nu}{\omega^2 + \nu^2 \omega} \right)^2 \right]^{1/2}. \quad (19)$$

By substituting  $X$  and  $Y$  into (12) and (13),  $\beta_p$  and  $\alpha_p$  can be simplified as

$$\beta_p = \frac{\omega}{c} \{X + Y\}^{1/2} \quad (20)$$

$$\alpha_p = \frac{\omega}{c} \{-X + Y\}^{1/2}. \quad (21)$$

We can solve (20) and (21) for  $X$  and  $Y$  in terms of  $\beta_p$  and  $\alpha_p$

$$X = \frac{c^2}{2\omega^2} (\beta_p^2 - \alpha_p^2) \quad (22)$$

$$Y = \frac{c^2}{2\omega^2} (\beta_p^2 + \alpha_p^2). \quad (23)$$

By inverting (18) and (19), we can calculate  $\nu$  as

$$\nu = 2\omega \frac{(Y^2 - X^2)^{1/2}}{(1 - 2X)} \quad (24)$$

and  $\omega_p$  as

$$\omega_p = [(1 - 2X)(\omega^2 + \nu^2)]^{1/2}. \quad (25)$$

Therefore, ultimately, we can write  $\nu$  and  $\omega_p$  in terms of the experimentally measured values  $\beta_p$  and  $\alpha_p$  by plugging the expression of  $X$  and  $Y$  in (22) and (23) into (24) and (25)

$$\nu = 2 \left( \frac{c^2}{\omega} \right) \left[ \frac{\alpha_p \beta_p}{1 - \frac{c^2}{\omega^2} (\beta_p^2 - \alpha_p^2)} \right] \quad (26)$$

$$\omega_p = \left\{ \left[ 1 - \frac{c^2}{\omega^2} (\beta_p^2 - \alpha_p^2) \right] \times \left[ \omega^2 + 4 \left( \frac{c^4}{\omega^2} \right) \left( \frac{\alpha_p \beta_p}{1 - \frac{c^2}{\omega^2} (\beta_p^2 - \alpha_p^2)} \right)^2 \right] \right\}^{1/2}. \quad (27)$$

The plasma frequency is related to electron density ( $\text{cm}^{-3}$ ) by

$$\omega_p = 2\pi \times 8.98 \times 10^3 \sqrt{n_e} \quad (28)$$

so we can calculate  $n_e$  from  $\omega_p$ . Equations (26) and (27) are inversions of (12) and (13). They are explicit and exact expressions of  $\omega_p$  and  $\nu$  with all the right-hand side terms known or measurable from interferometer.

In our plasma interferometry experiment, we first measure phase shift  $\Delta\varphi$  and relative attenuation  $A/A_0$  using interferometer, then use (16) and (17) to calculate the  $\beta_p$  and  $\alpha_p$  values, then calculate the plasma characteristics  $\nu$ ,  $\omega_p$ , and  $n_e$  from the calculated  $\beta_p$  and  $\alpha_p$  values using (26)–(28).

The quantities  $\nu$ ,  $\omega_p$ , and  $n_e$  were derived in an earlier work [30] using approximations of (12) and (13) for highly and weakly collisional cases. Since neither of these approximations is valid in the present experiment, it is necessary to use the exact expressions we have derived above. No approximation is used to derive (26) and (27) so they are exact solutions of  $\nu$  and  $\omega_p$  which can be used to calculate  $\nu$  and  $n_e$  from a wide range of experiments in which interferometry is available. Axial profiles of the plasma characteristics can also be obtained using this method.

The interferometer technique and method of analysis was previously compared with a Langmuir probe to obtain line-average density measurements in a lower pressure helicon plasma source over a wide range of densities and magnetic fields. The two measurements were found to be in agreement within 8% over a density range from  $4 \times 10^{12}/\text{cm}^3$  to  $1.5 \times 10^{13}/\text{cm}^3$  [31].

In addition to the evaluation of line average  $\omega_p$ ,  $n_e$ , and  $\nu$ , we have developed a method for determining the line-average electron temperature ( $T_e$ ) using plasma interferometry based on (11) utilizing the measured total electron–neutral collision frequency. The total electron cross section  $\sigma$  depends on the electron thermal energy: The total electron–neutral collision cross section curves generalized by Zecca *et al.* [29] are used to solve this equation for  $T_e$ . We used fifth-order polynomial functions to fit these experimental cross section data curves over a range from 0.1 to 2.5 eV and obtain  $\sigma$  as a function of  $E_{\text{eav}}$  for use in (11). From (7),  $T_n$  is found for the laser-RF plasmas we produce and  $n_n$  is obtained using (8). An iterative root-finding routine is needed to solve (11) for  $T_e$  using this method.

### C. Plasma Impedance Diagnostic and Optimization of RF Matching

One important advance that allows us to create fast, pulsed, high-pressure plasmas with lower RF power levels is a real-time plasma impedance measurement technique that we have developed that allows efficient matching of the 50- $\Omega$  RF network to the time varying plasma load. We define the plasma-loaded helical antenna radiation impedance  $Z_p(t) = R_p(t) + jX_p(t)$  (also referred to as the plasma impedance) as the impedance measured at the input to the antenna feeds from the capacitive matchbox. This impedance is a function not only of the character of the matchbox and helix itself, but also of the plasma initiated by the laser and sustained by the RF pulse. We write  $Z_p(t)$  as a function of time, meaning the RF plasma load is a function of time during the entire laser initiation and RF sustainment sequence. Before the 20-ns laser pulse ionizes the TMAE seed plasma, the chamber is filled with neutral gas that behaves essentially like a vacuum ( $\mu_0, \epsilon_0$ ). The antenna impedance without the plasma is given by  $Z_a = R_a + jX_a$ . Immediately after the laser pulse and the 100 ns delayed ionization process [17], the plasma is formed in the chamber and sustained by the RF power. During this time the laser pulse can lead to high-pressure plasma fluctuations that are observed visually. The dielectric properties of the plasma are substantially different from the vacuum antenna load. The permittivity of the plasma depends on  $n_e$  and  $\nu$  of the plasma, both of which vary substantially during the RF sustainment period due to transient behavior of the high-pressure plasma. As a result, the RF load  $Z_p(t)$  will exhibit a very fast transition when the plasma is initiated by the laser and varies in time due to the high-pressure plasma fluctuations and plasma recombination processes. It is of considerable interest to obtain  $Z_p(t)$  because the knowledge of plasma impedance provides the information that allows us to tune the capacitors for optimal RF matching during the RF pulse. This is crucial to achieve a high-RF-power coupling efficiency rapidly in a pulsed plasma and to protect the high-power RF generator from reflected power. Optimal matching can reduce the RF power levels, weight, and cost requirements for making pulsed high-pressure plasmas by measuring the RF load impedance in real-time to enable good matching of the final-stage steady-state plasma load to the 50- $\Omega$  RF impedance network.

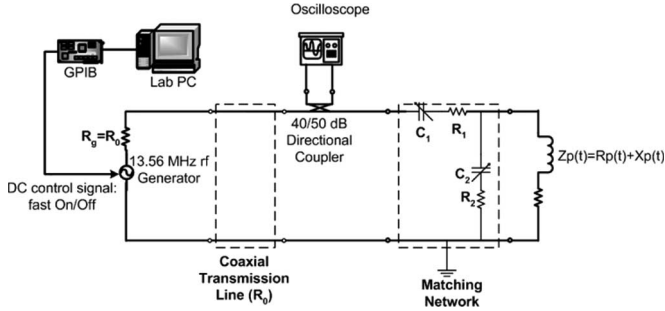


Fig. 2. Diagram of the RF coupling circuit and diagnostics.

We measure the plasma impedance *in situ* and in real-time using a dual directional coupler. The incident and reflected voltages ( $V_{in}$  and  $V_{ref}$ ) are measured by the coupler connected to the oscilloscope (as in the RF circuit diagram shown in Fig. 2), so that the input reflection coefficient  $\Gamma_{in}$  is found as  $\Gamma_{in} = V_{ref}/V_{inc}$ .  $Z_{in}$ , the input impedance looking into the match box, is calculated as  $Z_{in}(t) = Z_0(1 + \Gamma_{in}(t))/(1 - \Gamma_{in}(t))$ .  $Z_p(t)$  is thus

$$Z_p(t) = \frac{Z_2(Z_{in}(t) - Z_1)}{Z_1 + Z_2 - Z_{in}(t)} \quad (29)$$

in which  $Z_1$  and  $Z_2$  are the impedances of the tunable capacitors  $C_1$  and  $C_2$ , characterized by network analyzer measurements. A Matlab program solves for the plasma impedances based on the  $V_{in}$  and  $V_{ref}$  data obtained by the oscilloscope. The plasma impedance value after the RF sustainment condition is obtained is used to determine the optimum  $C_1$  and  $C_2$  settings, so that we substantially improve the impedance matching and minimize reflected RF power for subsequent pulses. This is thus an iterative procedure, in which first the two capacitors are set to some neutral position so that a plasma can be formed by laser initiation and RF sustainment. Then, a laser/RF pulse is applied using the desired plasma conditions including gas pressure, gas flow and RF power level from which a data set from the directional coupler is obtained. Although a plasma may form, a mismatch may occur resulting in as high as 40% RF power reflection. With the  $V_{inc}(t)$  and  $V_{ref}(t)$  data obtained, (29) can be used to calculate antenna radiation impedance  $Z_p(t)$ . With  $Z_p(t)$  calculated for this run, we can calculate the optimum  $C_1$  and  $C_2$  for the plasma sustained by RF and tune the capacitors accordingly for subsequent experimental runs. The result is very satisfactory. For 760-torr argon plasma, we are able to reduce the RF power reflection coefficient ( $|\Gamma|^2$ ) to 20%, and for a 50-torr nitrogen plasma,  $|\Gamma|^2$  is reduced to 6% for the final RF sustainment stage of the plasma. The reason that reflections cannot be reduced below 20% for 760-torr argon plasma is that the argon antenna plasma resistance experiences a large change from 0.5 to 5  $\Omega$  as the quasi-steady-state plasma is formed. Due to this large change in plasma impedance, it is not possible to tune for a perfect match for the final quasi-steady-state plasma impedance because if this is done, the mismatch level at the initiation of RF power will be too high. This mismatch makes it impossible for the RF

plasma to form and causes a high level of power reflection, activating the foldback protection mechanism of the RF generator which limits the actual output level of the generator to protect the unit itself. For the 50-torr nitrogen plasma experiment, due to a smaller change (from 0.5 to approximately 2  $\Omega$ ) in resistive antenna impedance, we can achieve a better matching with only a 6% RF power reflection coefficient. The exact RF power coupled to plasma  $P_e$  is obtained by excluding from  $P_{net}$  the matchbox and antenna losses using the  $e_{Ohm}$  and  $e_{Rad}$  factors as discussed in Section II-A.

#### D. Optical Emission Spectroscopy

Optical emission spectroscopy is used to characterize the temporal evolution of the plasma. The optically emitted spectral lines illustrate the temporal plasma evolution from a TMAE seed plasma initiated by the laser and early RF power to the quasi-steady-state RF plasma of neutral background gases such as argon and nitrogen. A three channel, wideband (200–850 nm) ST2000 Ocean Optics Spectrometer is used to record the plasma spectral emission perpendicular to the plasma column axis. Each channel is connected to a separate grating spectrometer (1200 lines/mm, with an optical resolution of 0.3 nm), which counts photons using a linear charge-coupled-device array (2048 pixels). Samples are taken over the following wavelength ranges: 200–500, 400–700, and 600–850 nm. The three-channel configuration has three centered blaze wavelength efficiency curves, which provides increased resolution over a single-channel model designed for the same wavelength range. The plasma spectral emission collected by a collimating lens is guided through optical fibers and focused on the detectors. The spectrometer output is connected to a PC with an A/D board and the data is acquired using a LabVIEW program developed by our group. The software provides more flexibility in operation and also allows for correction of spectral attenuation of the fiber optics. The program also controls the triggering of the laser source, the optical system, and the fast digital oscilloscope for data acquisition with accurate timing. The synchronized LabVIEW program triggers the spectrometer to acquire the optical emission at a specified time within the RF pulse, with 50-ms integration time to obtain good signal to noise ratio. By triggering the spectrometer at a specified time, the spectral emission of the early laser-initiated seed plasma and later quasi-steady-state RF plasma can be obtained, to diagnose the plasma evolution.

## IV. RESULTS AND DISCUSSION

Using the experimental and diagnostic methods detailed in Section III, we have been able to generate and analyze large volume 760-torr argon and 50-torr nitrogen plasmas. The results are presented as follows.

#### A. Optical Emission Measurements

In a typical pulsed argon plasma sequence, 2.2-kW net RF power coupled to the plasma (after subtracting losses from matching system, Ohmic heating of the antenna, and radiation

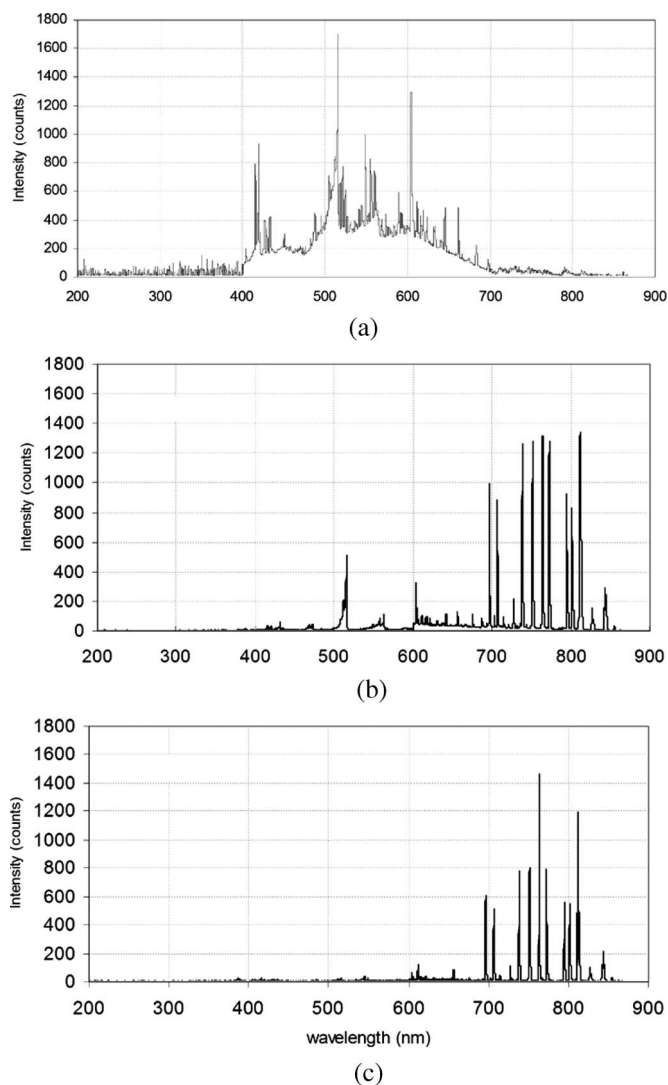


Fig. 3. Temporal evolution of early TMAE seed plasma and later quasi-steady-state RF argon plasma emission spectrum: (a)  $t = 50$  ms; (b)  $t = 200$  ms; (c)  $t = 400$  ms.

loss to the outside RF field) is used in conjunction with the 100-mJ laser pulse and 15-mtorr TMAE seed gas to initiate and sustain the plasma. The gas pressure of argon is 760 torr, which is maintained by 4.5-SLM flow rate. The valve of the mechanical pump is carefully set to balance the input gas and provide a steady chamber pressure of 760 torr. The spectrometer is triggered to capture the broad (200–800 nm) spectrum at three different times during the 1-s RF pulse with an integration time of 50 ms. The 20-ns laser pulse is fired at  $t = 50$  ms. The captured spectrums are shown in Fig. 3(a)–(c) which illustrate the transition from the TMAE seed plasma to the argon quasi-steady-state plasma. Fig. 3(a) shows the broad emission spectrum of the TMAE seed gas molecule at  $t = 50$  ms. The seed plasma dominates the entire spectrum early in the pulse. Fig. 3(b) shows that at  $t = 200$  ms the argon lines begin to dominate the spectrum. At  $t = 400$  ms as shown in Fig. 3(c), the quasi-steady-state argon plasma is reached with negligible seed gas presence. Thus, the laser ionization of the TMAE seed gas and transition to argon plasma is readily accomplished with our system.

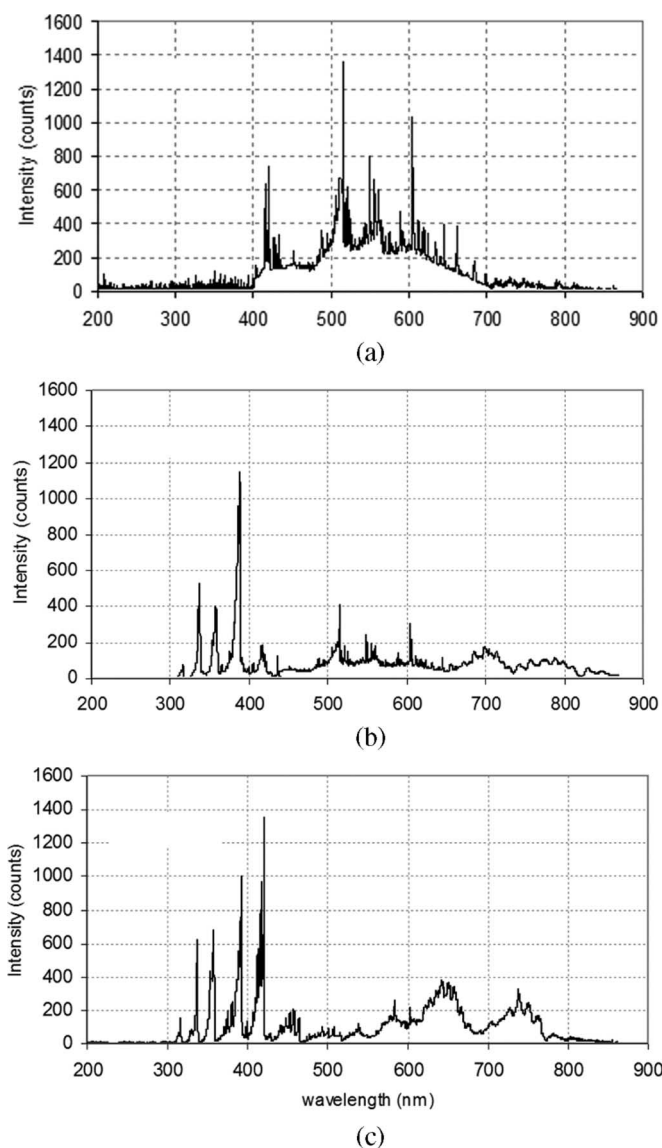


Fig. 4. Temporal evolution of early TMAE seed plasma and later quasi-steady-state RF nitrogen plasma emission spectrum: (a)  $t = 50$  ms; (b)  $t = 100$  ms. (c)  $t = 300$  ms.

In a typical pulsed nitrogen plasma sequence, 3.5-kW net RF power is coupled to the plasma in conjunction with the 100-mJ laser pulse and 15-mtorr TMAE seed gas to initiate and sustain the nitrogen plasma at 50-torr pressure, corresponding to atmospheric pressure at 60 000 feet altitude. The net RF power coupled into the plasma is found to be 3.5 kW after subtracting losses from the matching system, Ohmic heating of the antenna (skin effect), and radiation loss to the outside RF field. The nitrogen gas pressure is 50 torr, maintained by a 1.5-SLM flow rate. The evolution of the optical emission spectrum in a 50-torr nitrogen plasma is very similar, and is shown in Fig. 4(a)–(c), which show the plasma emission at  $t = 50, 100,$  and  $300$  ms with laser pulse set at  $t = 50$  ms.

### B. Argon Plasma

The argon plasma condition has been described in Section IV-A. RF power and plasma impedance experiment

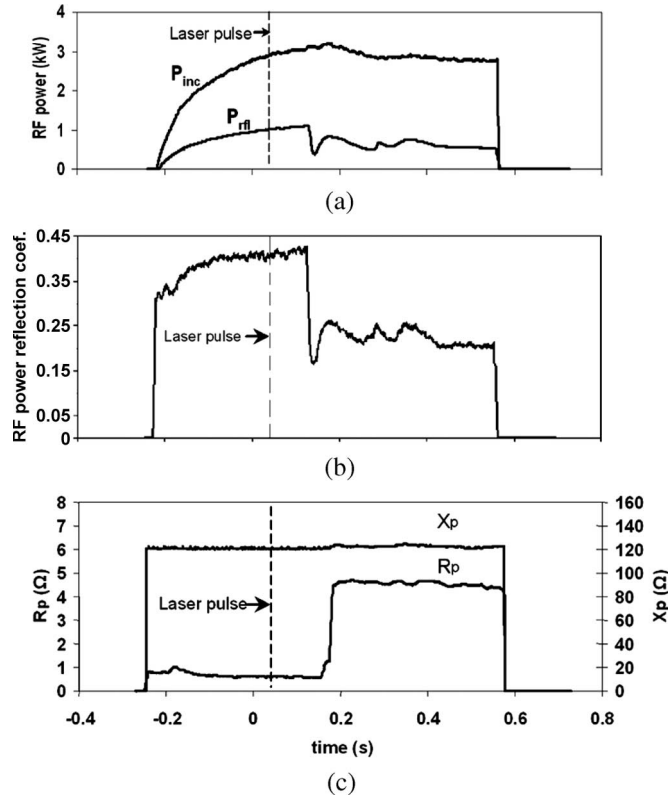


Fig. 5. (a) Incident and reflected RF power over a typical pulsed laser and RF generated argon plasma sequence. (b) Temporal variation of RF power reflection coefficient over the pulsed argon plasma sequence. (c) Temporal variation of  $R_p$  and  $X_p$  of this pulsed argon plasma sequence. The plasma condition is described in Section IV-A.

results are presented. Temporal as well as axial variation of plasma characteristics are diagnosed and presented in this section.

1) *RF Power and Plasma Impedance Measurements:* The dual directional coupler shown in Fig. 2 is used to measure  $P_{inc}$  and  $P_{ref}$  with results presented in Fig. 5(a). The net RF power coupled to the matchbox and antenna,  $P_{net} = P_{inc} - P_{ref}$ . The RF power reflection coefficient is  $|\Gamma|^2 = P_{ref}/P_{inc}$  as presented in Fig. 5(b).  $P_{net}$  is 2.5 kW during the final quasi-steady-state plasma stage and  $|\Gamma|^2 \approx 20\%$ . In order to obtain the RF power efficiency of the matchbox and helical antenna, we used the method discussed in Section II-A and obtain  $e_{Ohm} = 96\%$  and  $e_{Rad} = 90\%$ . Therefore, ultimately a power of  $P_e = 2.2$  kW is coupled to the steady-state argon plasma electrons.

One important aspect of RF sustainment of the laser-initiated plasma is to ensure that the RF matching is very good over the majority of the pulse, so that high-RF-power coupling efficiency can be achieved and the RF generator can be protected from high levels of reflected power. In order to achieve good matching, the temporal RF impedance variation is calculated using (29) based on directional coupler measurement of  $V_{inc}(t)$  and  $V_{ref}(t)$  over the RF plasma pulse. The plasma impedance  $Z_p(t) = R_p(t) + jX_p(t)$  is presented in Fig. 5(c). It is observed that  $R_p$ , the resistive load, exhibits a transition from 0.50 to 5.0  $\Omega$  when the quasi-steady-state plasma is formed at  $t = 183$  ms, while the inductive load  $X_p(t)$  shows a fractional increase of 2.0  $\Omega$ . This changing load means we have to deal



Fig. 6. Intermediate formation stage of the argon plasma.

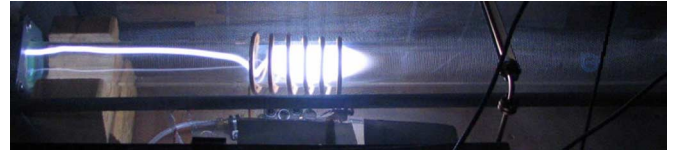


Fig. 7. Quasi-steady-state stage of argon plasma.

with two very different plasma load impedance levels during the pulse. We typically set the matching network to match the impedance of the quasi-steady-state plasma ( $5.0 + j120 \Omega$ ) to the 50- $\Omega$  generator, and allow a higher reflection level at the beginning of the pulse when the quasi-steady-state plasma is not formed. The RF generator can accept reflected power for a certain duration because of its high foldback reflected power tolerance of 5.0 kW. With this impedance measurement and matching technique, we obtain a 20% RF power reflection during the quasi-steady-state plasma despite the significant variation in plasma impedance during the plasma formation (from  $0.50 + j118$  to  $5.0 + j120 \Omega$ ).

2) *Time-Resolved Electron Density and Total Electron-Neutral Collision Frequency:* It is observed that the laser-initiated RF-sustained TMAE-seeded argon 760-torr plasma goes through two distinct stages. The RF power is initiated at  $t = -210$  ms and the laser pulse is triggered when the incident RF power output reaches approximately 90% of the maximum value (at  $t = 50$  ms): the tube powered RF generator needs  $\sim 260$  ms to ramp up its power output. Note that since we set the oscilloscope to trigger at the initial laser power supply charging, the laser actually fires at  $t = 50$  ms because it requires a 50-ms charging delay before firing. In other words, the RF power ramps up to 90% of its maximum power 260 ms after the RF pulse is triggered, at which time the laser is fired to form the initial seed plasma. The 20-ns laser pulse produces a high-density plasma [17] with  $n_e = 5.0 \times 10^{12} - 10^{13}/\text{cm}^3$  with a  $2.8 \times 1.2\text{-cm}^2$  cross-sectional area that is observable on the interferometer as a spike with a decay on the hundreds of microseconds time scale. Immediately after the laser plasma pulse is formed, a narrow plasma is formed under the antenna that fluctuates spatially, as shown photographically in Fig. 6. This is the intermediate formation stage of the plasma. Figs. 6 and 7 are taken at  $t = 50$  and 400 ms using exposure time 10 ms. Note that the laser pulselength is 20 ns, so the RF electric field is dominant for this plasma. The plasma is intense and sustained by the RF electric field. The less dense but bright track between region under the helical antenna and end plate on the left side is due to the large potential drop between the plasma core and the conducting end plate. During a typical RF pulse, this stage lasts 133 ms (from  $t = 50$  ms to  $t = 183$  ms on the time axis of Figs. 5 and 8).

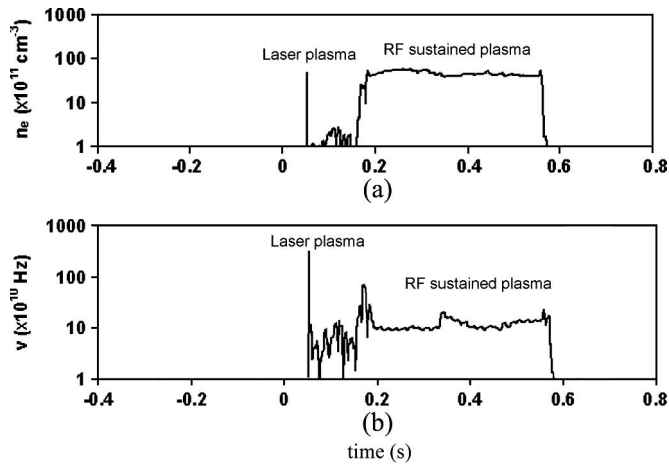


Fig. 8. (a) Temporal variation of electron density of the pulsed argon plasma sequence. (b) Temporal variation of total electron–neutral collision frequency of the pulsed argon plasma.

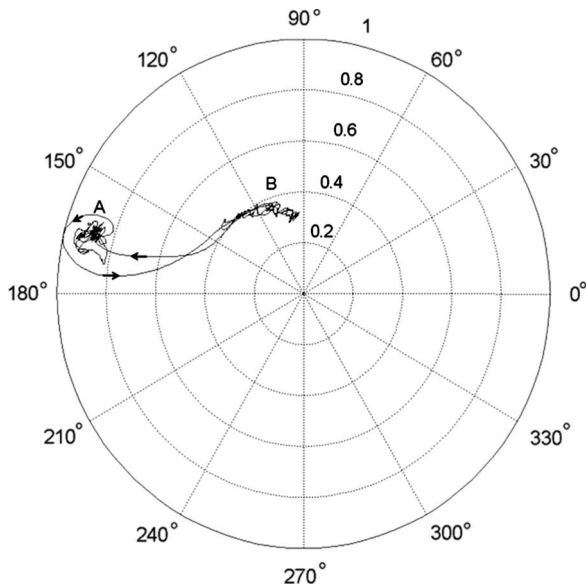


Fig. 9. Interferometer trace of a laser plus RF argon plasma sequence.

At  $t = 183 \text{ ms}$  (133 ms after the laser pulse), the plasma evolves into a quasi-steady-state high-density large-volume argon plasma (Fig. 7) which is sustained for 400 ms (until  $t = 581 \text{ ms}$  when RF power is turned OFF) and is readily diagnosed by the interferometer. In the RF power figures [Fig. 5(a) and (b)], a sharp fall in the RF power reflection coefficient is observed roughly at  $t = 183 \text{ ms}$ , corresponding to the formation of the quasi-steady-state stage of the plasma which is stable, has large volume and high density and has good RF coupling efficiency. The transition into the quasi-steady-state plasma stage is also observed in the interferometer signal (Fig. 8) as a rise in  $n_e$  and  $\nu$  which stabilize at elevated values during this stage of plasma. We examine the characteristics of this stage of the plasma using the method outlined in Section III-B. When the plasma is formed, the 5.0-cm line-average electron density and total electron–neutral collision frequency are diagnosable using the interferometer signals. The two signals (in-phase and

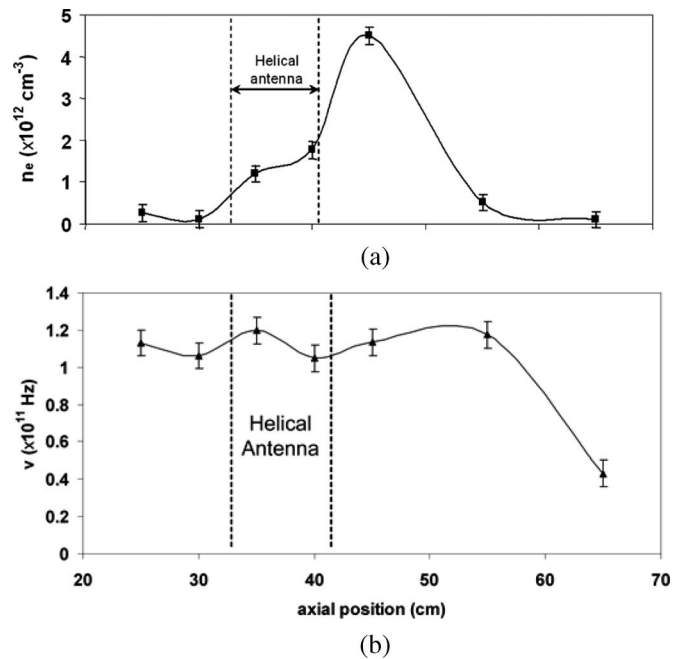


Fig. 10. Axial profile of plasma characteristics of the argon plasma: (a) electron density; (b) total electron–neutral collision frequency. The two dashed lines mark the position of two ends of the helical RF antenna. The same applies to Fig. 15.

quadrature-phase) from the interferometer are acquired by two channels of the oscilloscope, which are used to extract the phase shift and attenuation of the wave after it propagates through the plasma. The raw interferometer trace in Cartesian complex coordinates (X-Y) is presented in Fig. 9 as a polar plot ( $r - \theta$ ) with in-phase signal plotted as X and quadrature-phase plotted as Y. In this polar plot, the radius corresponds to the normalized wave amplitude (maximum = 1.0) while angle corresponds to the phase angle of the signal relative to the reference signal. Details of this method are presented in [30]. Point A corresponds to the vacuum millimeter wave signal before the plasma is initiated. Point B corresponds to wave launched through the quasi-steady-state plasma created by laser initiation and RF sustainment with delayed phase and dampened amplitude compared with A. The trace makes a transition from point A to B when the quasi-steady-state plasma is formed at  $t = 183 \text{ ms}$ , then back to A when the RF power is turned OFF at  $t = 581 \text{ ms}$ . Using the previously discussed mathematical method, the time-resolved  $n_e$  and  $\nu$  results are calculated and presented in the Fig. 8 (a) and (b). The resulting line-average  $n_e$  is  $4.5 \times 10^{12} \text{ cm}^{-3}$ , and  $\nu$  is  $1.1 \times 10^{11} \text{ Hz}$  at  $z = 44 \text{ cm}$  axial position, with  $z = 0$  defined at the laser window of the plasma chamber (Fig. 1). Even after the plasma reaches quasi-steady-state, we still observe some fluctuation in these measurements due to instabilities in high-pressure plasmas that has been discussed by other researchers [6], [11].

3) *Axial Profile of the Electron Density and Total Electron–Neutral Collision Frequency:* The axial profile of the line-average plasma characteristics  $n_e$  and  $\nu$  are diagnosed and presented in Fig. 10. As shown in the figures, we have achieved a high-pressure argon plasma that extends axially from the

helical antenna. The peak density occurs at  $z = 44$  cm, about 4.0 cm downstream from the helical antenna and the plasma extends approximately 15 cm beyond the antenna. Significant reduction in RF power levels required to sustain large volume high-pressure argon discharges was achieved using the laser initiation technique compared to that required for RF only plasma initiation and sustainment. Within the 500-cm<sup>3</sup> plasma volume that extends 25 cm axially, a volume average electron density of  $2.0 \times 10^{12}$  cm<sup>-3</sup> is achieved with 4.4 W/cm<sup>3</sup> steady-state RF power budget. The seed plasma also provides a good load for efficient RF coupling at lower power levels via rapidly pulsed, inductively coupled sources.

4) *Electron Temperature*: To evaluate  $T_e$ , we iteratively solve (11) for  $T_e$  based on the measured line average total electron–neutral collision frequency of  $1.1 \times 10^{11}$  Hz. Since  $P_e$  is 2.2 kW, and  $\eta$  is taken to be 40% for our case, which is based on detailed simulations and experimental work on argon neutral heating in ICP sources [22], [24], [25], a total of 880 W of net RF power contributes to neutral heating in the 500 cm<sup>3</sup> argon plasma. Using (7) and (8), the neutral temperature is found to be 1100 K. The neutral pressure is measured to rise by 50% from 760 to 1100-torr using the fast-response piezoelectric pressure gauge when the plasma reaches quasi-steady state. We assume that the chamber pressure reaches equilibrium within very short time scales compared to the RF pulselength. Thus, the pressure measured downstream using the piezoelectric gauge is an accurate representation of the gas pressure in the plasma region. Ultimately, after the neutrals are heated for 400 ms by the elastic electron–neutral collisions, the neutral density in the plasma region decreases to 39% of the room temperature density value at 760-torr pressure. The left- and right-hand sides of (11) are plotted in Fig. 11 using the measured  $\nu$  value and total electron collision cross section data generalized by Zecca *et al.* [29]; the intersection yields the electron temperature  $T_e = 0.86$  eV at  $z = 44$  cm axial position. The high-pressure plasma we make is categorized “quasi-steady-state” plasma because the electrons reach steady-state when the plasma is stabilized, but the neutrals continuously gain thermal energy from electrons through collisions and hence do not reach steady-state within the 400-ms plasma pulse.

C. Nitrogen Plasma

The nitrogen plasma condition is presented in detail in Section IV-A. A similar set of techniques as used for the argon plasma is used for the nitrogen plasma experiment to obtain RF power, plasma impedance, electron density, total electron collision frequency and electron temperature results.

1) *RF Power and Plasma Impedance*: The transition in resistive plasma impedance from the intermediate to quasi-steady-state plasma stage also occurs in the nitrogen plasma, but it is of lower magnitude due to the lower plasma density compared to the argon plasma: the resistive load increases from vacuum level of 0.50 to 2.0  $\Omega$  when the quasi-steady-state plasma is formed [Fig. 12(c)] which has a lower electron density compared with argon plasma. This smaller variation results in better RF matching for the nitrogen plasma. A remarkably low RF power reflection coefficient of 6.0% is achieved for

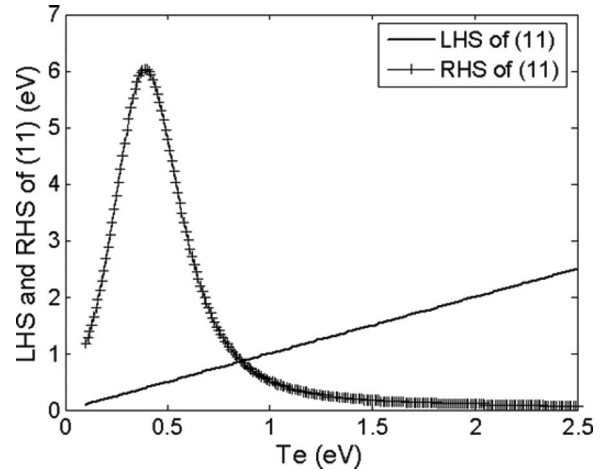


Fig. 11. Iterative solution of (11) for argon plasma.

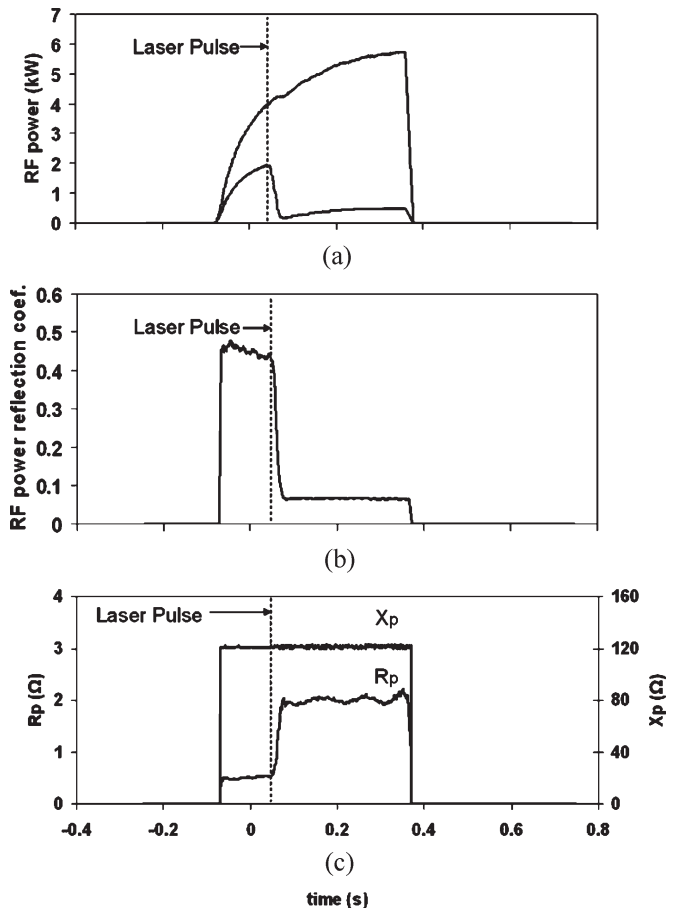


Fig. 12. (a) Incident and reflected RF power over a typical pulsed laser and RF generated nitrogen plasma sequence. (b) Temporal variation of RF power reflection coefficient over the pulsed nitrogen plasma sequence. (c) Temporal variation of  $R_p$  and  $X_p$  of this pulsed nitrogen plasma sequence. The plasma condition is described in Section IV-A.

the quasi-steady-state nitrogen RF plasma because we tune the matching network according to the steady-state plasma impedance. The RF power coupled into the matchbox and antenna  $P_{net}$  is 5.0 kW during the quasi-steady-state plasma stage. The RF power efficiency of the matchbox and helical

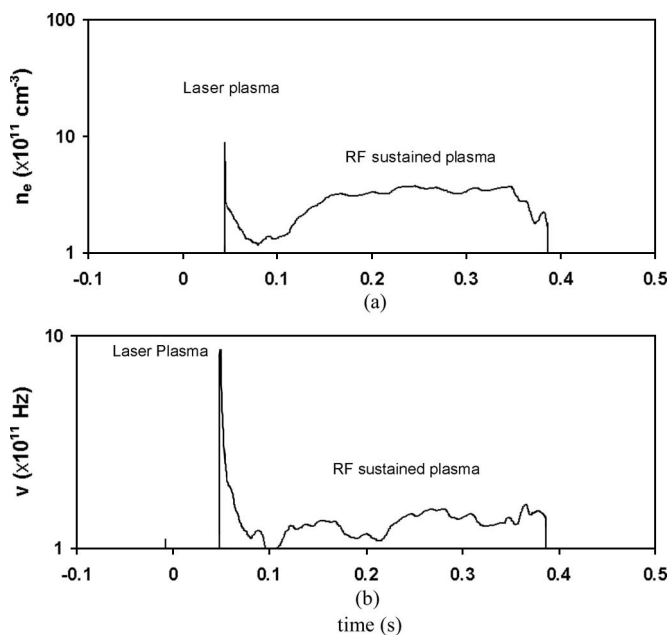


Fig. 13. (a) Temporal variation of electron density of the pulsed nitrogen plasma sequence. (b) Temporal variation of total electron–neutral collision frequency of the pulsed nitrogen plasma.

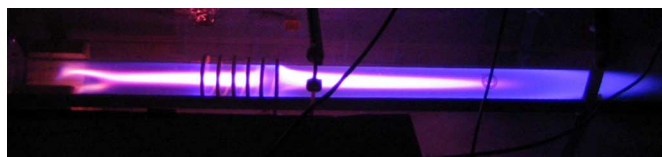


Fig. 14. Quasi-steady-state stage of nitrogen plasma.

antenna are found to be  $e_{\text{Ohm}} = 93\%$  and  $e_{\text{Rad}} = 75\%$ , respectively. Therefore, ultimately a  $P_e$  of 3.5 kW is coupled into the steady-state nitrogen plasma electrons. At lower pressure, the lower pressure nitrogen plasmas show much less temporal fluctuation in plasma characteristics than the argon plasma.

2) *Time-Resolved Electron Density and Total Electron–Neutral Collision Frequency:* The 50-torr nitrogen plasma exhibits a lower line-averaged electron density of  $3.5 \times 10^{11} / \text{cm}^3$ , but similar collision frequency of  $\nu \sim 1.2 \times 10^{11} / \text{s}$  (Fig. 13) when compared with the argon plasma. The density and collision frequency are measured at the peak density position of  $z = 44 \text{ cm}$ , 3 cm from the end of the antenna. The RF power is turned on at  $t = -70 \text{ ms}$ , then the laser is fired at  $t = 50 \text{ ms}$  creating a seed plasma represented by a spike in the interferometry signal shown in Fig. 13. As shown in Figs. 12 and 13, the duration of the intermediate formation stage lasts approximately 50 ms, much less than that of the argon plasma due to the lower neutral pressure. The electron density and total electron–neutral collision frequency fluctuate significantly during this plasma stage and  $\nu$  cannot be measured because the interferometer signal goes below the detectable range of the instrument. The quasi-steady-state nitrogen plasma is formed at  $t = 100 \text{ ms}$ . This plasma also exhibits some instabilities that are not uncommon in higher pressure discharges. The quasi-steady-state nitrogen plasma created has strong optical emis-

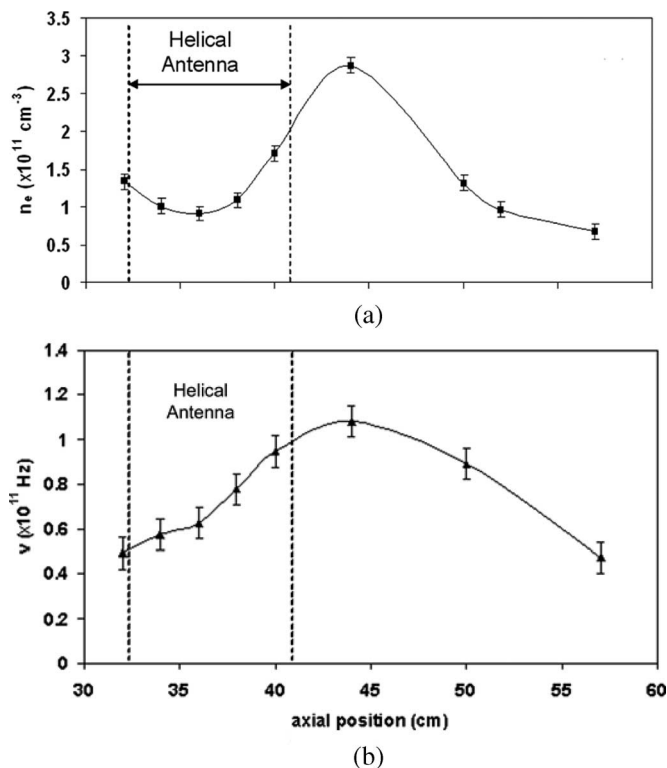


Fig. 15. Axial profile of plasma characteristics of the nitrogen plasma: (a) electron density; (b) total electron–neutral collision frequency.

sion (Fig. 14). The picture is taken at  $t = 300 \text{ ms}$  with 10 ms exposure time. It has a very bright purple core surrounded by dimmer blue peripheral region. The single-photon 193-nm excimer laser’s direct and delayed ionization substantially enhances the RF penetration away from the helical antenna.

3) *Axial Profile of the Electron Density and Total Electron–Neutral Collision Frequency:* The axial profiles of line average  $n_e$  and  $\nu$  are presented in Fig. 15. The nitrogen plasma density also exhibits a bell-shaped axial profile. The interferometer result suggests that the plasma extends 25 cm axially. However, visually the plasma extends 75 cm along the chamber axis (Fig. 14). This discrepancy is because the interferometer can only detect density within the range between  $10^{11}$  and  $10^{14} \text{ cm}^{-3}$  (when  $n_e$  is below the lower limit, the phase shift of the millimeter wave is too small to be detected, and above the upper limit, the millimeter wave is cutoff by the plasma), and the plasma outside the detectable region has a density below  $10^{11} \text{ cm}^{-3}$  although it has strong optical emission. If we assume a quasi-linear axial density profile within the  $1500\text{-cm}^3$  visible plasma volume that extends 75 cm axially, a volume average  $n_e$  of  $5.0 \times 10^{10} \text{ cm}^{-3}$  and  $\nu$  of  $0.80 \times 10^{10} \text{ Hz}$  is achieved with the  $2.3\text{-W/cm}^3$  RF power budget.

4) *Electron Temperature:* We iteratively solve (11) for the line average  $T_e$  based on the measured total electron–neutral collision frequency. The total heating efficiency factor  $\eta$  of nitrogen plasma is taken to be 20%. Numerous inelastic processes that compete with neutral heating occur in high-pressure nitrogen plasmas [26], reducing the neutral heating fraction. Using (7) and (8), the neutral temperature is found to be 2400 K. The

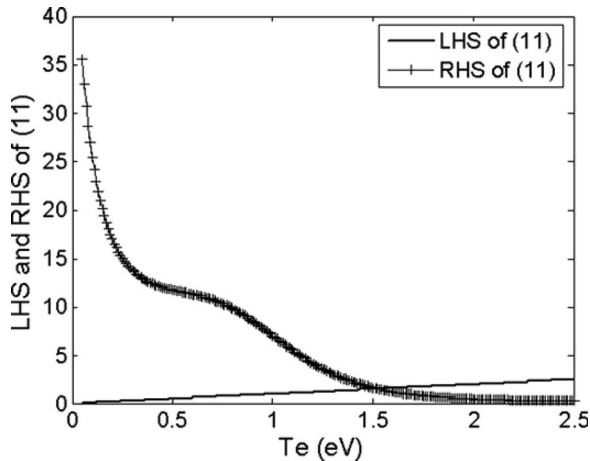


Fig. 16. Iterative solution of (11) for nitrogen plasma.

neutral pressure is measured to rise from 50 to 90 torr using the piezoelectric pressure gauge when the plasma is stabilized and sustained. As a result of neutral heating, the neutral density decreases to 22% of the room temperature density value at 50-torr pressure. The left- and right-hand sides of (11) are plotted in Fig. 16, so  $T_e$  is found to be 1.5 eV at  $z = 44$  cm axial position.

## V. DISCUSSION AND SUMMARY

A technique for creating and diagnosing electrodeless high-pressure large-volume ( $\geq 500$  cm) plasmas in argon (760 torr) and nitrogen (50 torr) is presented. The use of the readily ionizable TMAE seed gas with UV excimer laser initiation allows the formation of plasma at high pressure of large volumes with substantially reduced RF power levels. Previous work by our group has shown that the UV excimer laser can penetrate well into the highly collisional TMAE plasma it creates [15], so a 100-cm-long TMAE plasma initial condition is made for efficient RF power coupling. Although the RF frequency  $f_{RF} = 13.56$  MHz is much less than the  $\nu \sim 10^{11}$  Hz total electron-neutral collision frequency, the laser-formed, long plasma initial condition allows better penetration of the RF power and creation of longer argon and nitrogen plasma that allows the plasma to project well beyond the helical coil than would be possible with RF power alone. Broadband optical spectroscopy is utilized to illustrate the transition from the TMAE-seeded laser-initiated plasma to the majority gas plasma later in the pulse sequence.

A technique to accurately measure the plasma impedance is discussed and demonstrated, which enables greatly improved RF matching via the two capacitor matching system with pulsed operation. Power reflection levels as low as 6.0% in nitrogen are achieved. Millimeter wave interferometry is used to diagnose the line average plasma density and total electron-neutral collision frequency: The argon plasma has maximum line-average electron density of  $4.5 \times 10^{12}$  cm $^{-3}$  and line-average total electron-neutral collision frequency of  $1.1 \times 10^{11}$  Hz; the nitrogen plasma has maximum line average electron density of  $3.5 \times 10^{11}$  cm $^{-3}$  and line average total electron-neutral

collision frequency of  $1.2 \times 10^{11}$  Hz. The maximum densities and collision frequencies occur 4-cm downstream from the helical antenna due to RF penetration and gas flow.

Utilizing an RF power budget of 4.4 W/cm $^3$ , we have been able to sustain a high density (a volume average electron density of  $2.0 \times 10^{12}$  cm $^{-3}$ ), 760-torr argon plasma for 400 ms that extends 25 cm axially and has a total plasma volume of 500 cm $^3$ . The nitrogen plasma that we obtained using the same technique extends approximately 75 cm axially, has 1500-cm $^3$  volume and requires an RF power budget of 2.3 W/cm $^3$  to sustain the volume average density of  $5.0 \times 10^{10}$  cm $^{-3}$  for 350 ms. If only RF power is used to initiate and sustain the argon and nitrogen plasmas, we can create pulsed plasmas at these power levels in argon below 50 torr and nitrogen below 10 torr, respectively. In these cases, the plasma volumes and RF penetration lengths are well below those for the laser-initiated plasmas: in argon, the plasma can only extend 15 cm axially (a 300-cm $^3$  volume); in nitrogen, it can only penetrate 25 cm (a 500-cm $^3$  volume). In addition, we have developed a new interferometer technique to evaluate the line average electron temperature in neutral dominated high-pressure plasmas. Based on assumed neutral heating efficiencies for argon and nitrogen, our RF power balance analysis and interferometer diagnostic technique yields an electron temperature of 0.86 eV in argon at 760 torr with  $T_n = 1100$  K and 1.5 eV in nitrogen at 50 torr with  $T_n = 2400$  K. Because  $T_n$  is evaluated just before the end of the RF pulse,  $n_n$  and  $T_e$  are also evaluated for the quasi-steady-state plasma just before the RF power is turned OFF. Following a plasma equilibrium analysis by Griem [32], an electron density higher than  $2 \times 10^{17}$  is needed for the plasmas with  $T_e$  greater than 0.8 eV to be in complete local thermal equilibrium (LTE). LTE means all the quantum states within the atoms or ions are in thermal equilibrium including the ground state. This gives additional validation to the experimental result of temperature difference between electrons and neutrals.

## ACKNOWLEDGMENT

The authors would like to thank Dr. K. Akhtar for many useful discussions, J. Morin of Comdel, Inc. for useful technical assistance on the RF generator, and Prof. S. Nelsen and G. Li of the Chemistry Department of the University of Wisconsin-Madison for their help in synthesizing TMAE.

## REFERENCES

- [1] P. Tsai, L. Wadsworth, and J. R. Roth, "Surface modification of fabrics using a one-atmosphere glow discharge plasma to improve fabric wettability," *Tex. Res. J.*, vol. 67, no. 5, pp. 359–369, 1997.
- [2] K. Kelly-Wintenberg, T. C. Montie, C. Brickman, J. R. Roth, A. K. Carr, K. Sorge, L. C. Wadsworth, and P. P. Y. Tsai, "Room temperature sterilization of surfaces and fabrics with a one atmosphere uniform glow discharge plasma," *J. Ind. Microbiol. Biotech.*, vol. 20, no. 1, pp. 69–74, Jan. 1998.
- [3] K. Kelly, J. E. Scharer, G. Ding, M. Bettenhausen, and S. P. Kuo, "Microwave reflections from a vacuum ultraviolet laser produced plasma sheet," *J. Appl. Phys.*, vol. 85, no. 1, pp. 63–68, Jan. 1999.
- [4] R. J. Vidmar, "On the use of atmospheric pressure plasmas as electromagnetic reflector and absorbers," *IEEE Trans. Plasma Sci.*, vol. 18, no. 4, pp. 733–741, Aug. 1990.

- [5] M. Laroussi, "Scattering of EM waves by a layer of air plasma surrounding a conducting cylinder," *Int. J. Infrared Millim. Waves*, vol. 17, no. 12, pp. 2215–2232, Dec. 1996.
- [6] K. H. Becker, U. Kogelschatz, K. H. Schoenbach, and R. J. Barker, *Nonequilibrium air plasmas at atmospheric pressure*. Bristol, U.K.: Inst. Phys., 2005.
- [7] R. J. Vidmar and K. R. Stalder, "Air chemistry and power to generate and sustain plasmas: Plasma lifetime calculations," in *Proc. AIAA*, 2003, pp. 1–8.
- [8] M. A. Lieberman and A. J. Lichtenberg, *Principles of plasma discharges and materials processing*, 2nd ed. New York: Wiley, 2005.
- [9] S. P. Bozeman and W. M. Hooke, "Magnetically enhanced electromagnetic wave penetration in weakly ionized plasmas," *Plasma Sources Sci. Technol.*, vol. 3, no. 1, pp. 99–107, Feb. 1994.
- [10] A. B. Petrin, "On the transmission of microwaves through plasma layer," *IEEE Trans. Plasma Sci.*, vol. 28, no. 3, pp. 1000–1008, Jun. 2000.
- [11] H. U. Eckert and F. L. Kelly, "Spectroscopic observations on inductively coupled plasma flames in air and argon," *J. Appl. Phys.*, vol. 39, no. 3, pp. 1846–1852, Feb. 1968.
- [12] G. I. Babat, "Electrodeless discharges and some allied problems," *J. Inst. Electron. Engrs. (London)*, vol. 94, pt. III, pp. 27–37, Jan. 1947.
- [13] C. H. Kruger, T. G. Owano, and C. O. Laux, "Experimental investigation of atmospheric pressure nonequilibrium plasma chemistry," *IEEE Trans. Plasma Sci.*, vol. 25, no. 5, pp. 1042–1051, Oct. 1997.
- [14] C. O. Laux, T. G. Spencer, C. H. Kruger, and R. N. Zare, "Optical diagnostics of atmospheric pressure air plasmas," *Plasma Sources Sci. Technol.*, vol. 12, no. 2, pp. 125–138, May 2003.
- [15] S. Ramakrishnan and M. W. Rogozinski, "Properties of electric arc plasma for metal cutting," *J. Phys. D, Appl. Phys.*, vol. 30, no. 4, pp. 636–644, Feb. 1997.
- [16] A. Schutze, J. Y. Young, S. E. Babayan, J. Park, G. S. Selwyn, and R. F. Hicks, "The atmospheric-pressure plasma jet: A review and comparison to other plasma sources," *IEEE Trans. Plasma Sci.*, vol. 26, no. 6, pp. 1685–1694, Dec. 1998.
- [17] K. Akhtar, J. Scharer, S. Tysk, and C. M. Denning, "Characterization of laser produced tetrakis (dimethylamino) ethylene plasma in a high-pressure background gas," *IEEE Trans. Plasma Sci.*, vol. 32, no. 2, pp. 813–822, Apr. 2004.
- [18] K. L. Kelly, J. E. Scharer, E. S. Paller, and G. Ding, "Laser ionization and radio frequency sustainment of high-pressure seeded plasmas," *J. Appl. Phys.*, vol. 92, no. 2, pp. 698–709, Jul. 2002.
- [19] G. Ding, J. E. Scharer, and K. Kelly, "Diagnostics and analyses of decay process in laser produced tetrakis (dimethyl-amino) ethylene plasma," *Phys. Plasmas*, vol. 8, no. 1, pp. 334–342, Jan. 2001.
- [20] K. L. Kelly, "Laser ionization and radiofrequency sustainment of high-pressure seeded plasmas," Ph.D. dissertation, Univ. Wisconsin, Madison, WI, 2001.
- [21] W. L. Stutzman and G. A. Thiele, *Antenna Theory and Design*, 2nd ed. Hoboken, NJ: Wiley, 1998, p. 43.
- [22] D. B. Hash, D. Bose, M. V. S. Rao, B. A. Cruden, M. Meyyappan, and S. P. Sharma, "Impact of gas heating in inductively coupled plasmas," *J. Appl. Phys.*, vol. 90, no. 5, pp. 2148–2157, Sep. 2001.
- [23] Y. P. Raizer, *Gas Discharge Physics*, Reprint ed. New York: Springer-Verlag, 1997.
- [24] S. K. Nam and D. J. Economou, "Two-dimensional simulation of a miniaturized inductively coupled plasma reactor," *J. Appl. Phys.*, vol. 95, no. 5, pp. 2272–2277, Mar. 2004.
- [25] M. W. Kiehlbauch and D. B. Graves, "Modeling argon inductively coupled plasmas: The electron energy distribution function and metastable kinetics," *J. Appl. Phys.*, vol. 91, no. 6, pp. 3539–3546, Mar. 2002.
- [26] M. Moravej, X. Yang, M. Barankin, J. Penelon, and S. E. Babayan, "Properties of an atmospheric pressure radio-frequency argon and nitrogen plasma," *Plasma Sources Sci. Technol.*, vol. 15, no. 2, pp. 204–210, May 2006.
- [27] F. F. Chen, *Introduction to Plasma Physics and Controlled Fusion*, 2nd ed. New York: Plenum Press, 1984.
- [28] I. P. Shkarofsky, T. W. Johnston, and M. P. Bachynski, *The Particle Kinetics of Plasmas*. Dordrecht, Netherlands: Addison-Wesley, 1966.
- [29] A. Zecca, G. P. Karwasz, and R. S. Brusa, "One century of experiments on electron-atom and molecule scattering: A critical review of integral cross sections," *Rivista Del Nuovo Cimento*, vol. 19, no. 3, pp. 1–146, 1996.
- [30] K. Akhtar, J. Scharer, S. Tysk, and E. Kho, "Plasma interferometry at high pressures," *Rev. Sci. Instrum.*, vol. 74, no. 2, pp. 996–1001, Feb. 2003.
- [31] S. Tysk, C. M. Denning, J. E. Scharer, and K. Akhtar, "Optical, wave measurements, and modeling of helicon plasmas for a wide range of magnetic fields," *Phys. Plasmas*, vol. 11, no. 3, pp. 878–887, Mar. 2004.
- [32] H. R. Griem, *Plasma Spectroscopy*, 1st ed. New York: McGraw-Hill, 1964.



**Siqi Luo** (M'05) received the B.S. degree in materials science from Shanghai Jiao Tong University, Shanghai, China, in 2001 and the M.S. degree in advanced materials from the Singapore-MIT Alliance Program, National University of Singapore, Singapore, in 2003. He is currently working toward the Ph.D. degree at the Department of Electrical and Computer Engineering, University of Wisconsin-Madison.

His industrial experience includes a graduate research internship with the Institute of Microelectronics, Singapore, in 2003 and an engineer position with Semiconductor Manufacturing International Corporation, Shanghai, in 2001. His research work focuses on experimental and computational study of the RF, microwave, and laser plasma technologies.

Mr. Luo was the recipient of the Institute of Materials Research and Engineering Award for Best Student for his M.S. work.



**John E. Scharer** (SM'90) received the B.S., M.S., and Ph.D. degrees in electrical engineering from the University of California, Berkeley, in plasma physics.

He is a Professor with the Department of Electrical and Computer Engineering and the Co-Director of the Center for Plasma Theory and Computation, University of Wisconsin-Madison. He has spent sabbaticals at the Commissariat à l'Énergie Atomique, Fontenay-aux-Roses, France, in 1970, the Joint European Torus, Culham, U.K., in 1983, and the

Australian National University, Sydney, Australia, in 2000, working on RF plasma physics. He has substantial research experience in excimer laser plasma creation, optical spectroscopy, radio frequency sustainment, millimeter-wave diagnostics, and chemistry of organic seed gas plasmas in air and microwave vacuum electronics. He also has extensive experience in theoretical, computational, and experimental researches on antenna coupling and wave propagation, as well as heating and creative diagnostics in plasmas and vacuum electronics.



**Magesh Thiyagarajan** (S'99) was born in Chennai, India, in 1981. He received the B.E. degree (with honors) in engineering from the University of Madras, Chennai, in 2001 and the M.S. degree (with the citation for professional promise) from the University of Tennessee, Knoxville, in 2004. He is currently working toward the Ph.D. degree in plasma and applied physics at the University of Wisconsin-Madison. His M.S. thesis focused on nonthermal large-volume atmospheric pressure plasmas, tunable plasma stealth antennas, and plasma ball lightning.

His current research interest is focused on laser-initiated and radio-frequency-sustained atmospheric pressure air constituent plasmas, as well as high-power laser-focused breakdown plasmas and optical diagnostics.

Mr. Thiyagarajan is a member of the engineering honor societies Tau Beta Pi, Eta Kappa Nu, and Order of the Engineer. He was the Vice President of the IEEE Chapter at Wisconsin-Madison (2004–2005). He was the recipient of the IEEE Graduate Student Scholarship Award in 2004.



**C. Mark Denning** (M'01) received the B.S. degree in electrical engineering from the University of Illinois at Chicago in 2002 and the M.S. degree in electrical engineering from the University of Wisconsin-Madison in 2004. He is currently working toward the Ph.D. degree at the Department of Electrical and Computer Engineering, University of Wisconsin-Madison.

His research interests include experimentation and computational modeling of helicon plasmas as well as high-pressure inductive discharges.